CHAPTER 21

An Overview of Radar Imaging

Gregory A. Showman

Chapter Outline

21.1 INTRODUCTION

Synthetic aperture radar (SAR) is a combination of radar hardware, waveforms, signal processing, and relative motion that creates photograph-like renderings of stationary targets and scenes of interest. The principal product of any basic SAR implementation is a fine-resolution two-dimensional intensity image of the illuminated scene. SAR is widely employed by the remote sensing community for mapping and land-use surveying and by the military for detection, location, identification, and assessment of fixed targets.

To motivate this discussion, Figure 21-1 shows two pictures of a portion of the Albuquerque Airport: one a traditional optical photograph (Figure 21-1b) and the other a SAR image (Figure 21-1a). A cursory comparison of these images suggests the phenomenologies in optical and radar imaging are similar; indeed, SAR can be thought of as a kind of "radar photography." However, a closer examination reveals significant differences.

For example, the optical photograph, recorded in daytime, is dominated by returns with significant reflectivity in the visible spectrum, so that white concrete tarmac appears bright while road and runway blacktop render dark. The SAR image, in contrast, highlights objects that reflect radar energy back to the radar. Smooth, flat, horizontal surfaces like roads and runways tend to reflect energy away from the radar, so these objects are dark in the SAR imagery. Buildings and vehicles are often constructed with metal components arranged in strongly retro-reflective geometries, causing these man-made objects to produce high intensities in the SAR image, thereby increasing their visibility in the scene compared with optical photographs.

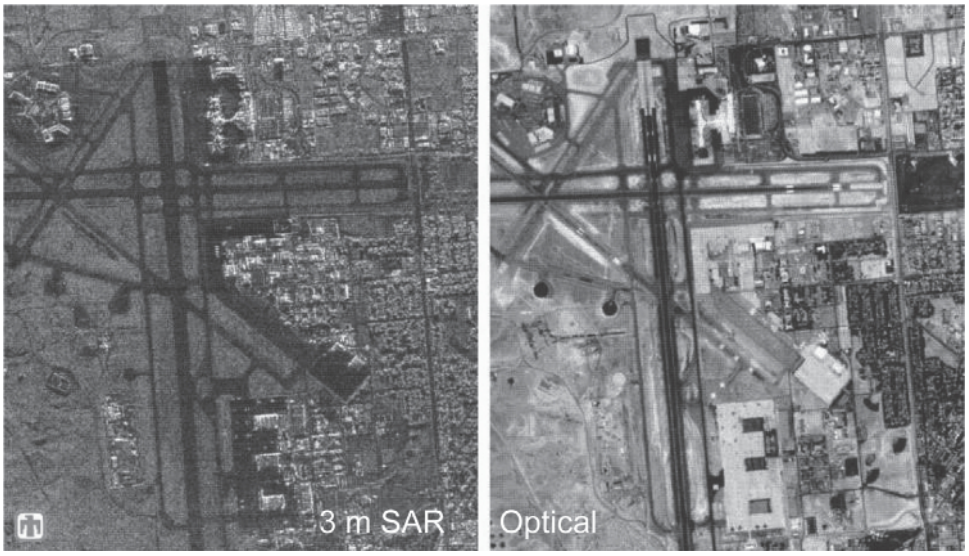

(a) (b)

FIGURE 21-1 ■ Two renderings of Albuquerque Airport. (a) Synthetic Aperture Radar image, and (b) optical overhead photograph. (Images courtesy of Sandia National Laboratories.)

As the reader is likely familiar with the process and product of optical photography, the following is a list of some of the advantages of SAR over this more traditional imaging method:

- SAR, by definition, is built around radar returns, which allows quality imagery to be generated at night and in inclement weather, conditions that thoroughly thwart optical imaging.
- SAR emphasizes man-made returns, an important consideration for many military and remote sensing applications.
- It will be seen that SAR systems have the potential for very fine resolutions, down to a few inches. Moreover, these resolutions can be maintained at long ranges without the need to dramatically expand or augment existing radar hardware.
- Radar operation at low center frequencies permits penetration of cover and concealment. For example, *foliage penetration* (FOPEN) SAR systems can image vehicles hidden beneath treetop canopies. *Ground penetration* (GPEN) SAR is capable of revealing the presence of objects buried underground.
- SAR requires coherent operation; that is, the radar system must be capable of measuring both amplitude and phase and must use waveforms with well-controlled phase characteristics. One consequence of coherent operation and processing is that each pixel in a SAR image is complex, possessing both amplitude and phase information. Specialized modes have been developed that exploit the phase information to estimate terrain and target heights or to detect subtle changes that have occurred in the imaged scene over time.
- Most radar systems transmit and receive radiofrequency (RF) energy at a single polarization. Some SAR systems are capable of transmitting and receiving multiple polarizations, resulting in multipolarimetric SAR imagery. The additional information provided by multiple polarizations has proven useful for land and foliage type classification and ground vehicle identification.

All of these benefits come at some price, of course. While not dependent on ambient light, the radar must provide the hardware to illuminate the scene of interest. Optical systems can snap a picture in a fraction of a second, whereas fine-resolution SAR systems can require several seconds, or even minutes, to collect enough data to form an image. Precise timing and phase control must be built into the radar hardware to ensure coherent operation over dwells that may last tens of seconds. Modern SAR image formation places challenging demands on the speeds and memories of digital signal processing hardware, while the associated software or firmware must implement, efficiently and with tightly managed approximations, sophisticated filters and transformations.

The goal of this chapter is to familiarize the reader with the operation and implementation of radar imaging in general and synthetic imaging in particular. Topics related to coherent imaging methods such as SAR include resolution relationships, sampling requirements, data collection considerations, and approaches to image formation. A complete mathematical development of the SAR system impulse response is used to derive both a simple but crude Doppler-based imaging method as well as a very general, high-fidelity, matched filtering technique. Next, phenomenologies and artifacts particular to radar images are discussed. Finally, several elementary SAR image quality metrics are introduced.

One last clarification on the scope of this chapter is provided here. Recall the fundamental product of any SAR data acquisition and processing operation is a two-dimensional image. Each dimension entails a distinct method of measurement and coherent integration. The first of these two dimensions, termed *down-range*, is plumbed via wideband waveforms and focused using the pulse compression and matched filtering techniques presented in detail in Chapter 20. Conversely, the emphasis of this treatment is on the orthogonal, *cross-range* dimension. It will be shown that cross-range information for a scene of interest is gathered through the motion of the SAR platform, while focusing of cross-range returns is achieved by applying measurements to a suitable image formation algorithm.

21.2 GENERAL IMAGING CONSIDERATIONS

SAR is typically presented using one of three paradigms:

1. SAR as a large synthetic antenna aperture.
2. SAR as range-Doppler imaging.
3. SAR as a signal processing exercise.

In this chapter, the first two paradigms are generally eschewed in favor of the signal processing view of SAR. However, for completeness, in this section all three approaches are reviewed.

21.2.1 SAR as a Large Synthetic Antenna Aperture

The concept of SAR as a means of forming a large synthetic antenna aperture is often found in traditional radar texts [e.g., 1,2]. This development begins by reviewing the noncoherent radar mapping mode known as *real-beam ground mapping* (RBGM). In RBGM a two-dimensional intensity map is made of a ground scene by first generating a one-dimensional

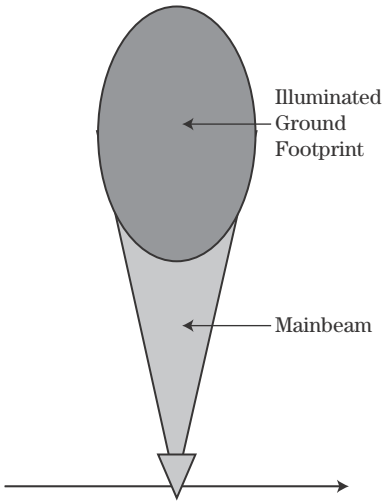

FIGURE 21-2 ■ Overhead view illustrates radar platform moving from left to right with side-looking antenna having main beam and ground footprint pointed towards the top.

range profile on a single pulse. Narrow range bins can be achieved by using short pulses or any of the wideband pulse compression techniques presented in Chapter 20. The return in any given bin is the coherent sum of the returns from all scatterers across the mainbeam extent at that particular range.

A two-dimensional map is produced by generating range profiles over a series of pulses and then placing the profiles next to one another in the order they were collected. The radar is operated so that the antenna illuminates a slightly different portion of the scene from pulse to pulse. For example, a stationary radar with a rotating antenna has a beam that sweeps through angle over time, and RBGM produces a two-dimensional intensity image as a function of slant range and azimuth angle. This polar-formatted data is often rendered using a plan position indicator (PPI) display.

When the goal is to survey large areas, a radar can be mounted on a vehicle with the antenna pointed to one side and oriented normal to the direction of travel, as seen in Figure 21-2. When the radar platform is an aircraft this arrangement is known as *side-looking airborne radar* (SLAR). In SLAR the antenna is not rotated; rather, the motion of the vehicle ensures a different portion of the earth's surface is illuminated from pulse to pulse. Scatterers in the scene drift into and out of the mainbeam as the aircraft moves along. The RBGM mode results in a map whose axes are the cross-track range to the scene and the along-track position of the aircraft. Cross-track range corresponds to the slant range to a bin in the range profiles and in radar imaging is sometimes known as "down-range." Displacement in the orthogonal direction, azimuthal for the stationary rotating radar, and along-track for the SLAR, is known generally as "cross-range."

The SLAR antenna beam pattern acts as a kind of low-pass filter, blurring scatterer returns in the cross-range direction of the image. The azimuth beamwidth of the antenna, then, sets a limit on the achievable image resolution. Note that the azimuthal extent of the beam on the ground is proportional to range, so that cross-range resolution gets worse as down-range increases. For a range R and a 3 dB azimuth beamwidth θ_3 (in radians), the cross-range resolution ΔCR is approximately

$$\Delta CR \approx R\theta_3 \tag{21.1}$$

Narrower beamwidths mean less blurring and finer resolutions. However, as discussed in Chapter 9, for a fixed operating wavelength, narrow beamwidths require large antennas. For an antenna length D and an RF wavelength λ, an approximate expression for the 3 dB beamwidth is

$$\theta_3 \approx \frac{\lambda}{D} \tag{21.2}$$

Combining (21.1) and (21.2) gives

$$\Delta CR \approx R\frac{\lambda}{D} \tag{21.3}$$

Equation (21.3) states that fine cross-range resolutions at long ranges require large antennas. Even moderate resolutions and ranges can quickly lead to antennas much too long to practically mount on a vehicle.

SAR can be thought of as an alternative solution to the "large antenna" problem. Instead of flying with a very large antenna, SAR uses a small antenna with a wide beam to collect radar returns from the scene as the aircraft flies along a straight line distance D_{SAR}, the SAR baseline. Once the measurements are recorded they are coherently combined to realize a synthetic aperture radar beamwidth θ_{SAR} consistent with the collection distance

$$\theta_{SAR} \approx \frac{\lambda}{2D_{SAR}} \tag{21.4}$$

Comparing equations (21.2) and (21.4), it can be seen that D_{SAR} is the length of a synthetic antenna aperture. (The factor of two appears in equation (21.4) because the transmit location moves with the platform, whereas the entire aperture is used on transmit in a real antenna. In essence, equation (21.4) is the beamwidth for a two-way pattern.) Substituting for the azimuth beamwidth in equation (21.1) with the SAR beamwidth in (21.4) yields the SAR version of (21.3),

$$\Delta CR \approx R\frac{\lambda}{2D_{SAR}} \tag{21.5}$$

By collecting data over longer distances, narrower SAR beamdwidths can be realized and fine cross-range resolutions achieved at long ranges.

SAR typically employs pulsed waveforms, so that the data recorded over D_{SAR} is collected at discrete, uniformly spaced locations determined by the platform velocity and radar pulse repetition frequency (PRF). This discretization along the synthetic aperture means SAR image formation can be roughly understood by resorting to the beam-steering developments for phased arrays or, more appropriately, digital arrays.

The large-aperture model becomes awkward when imaging at fine resolution or low frequencies. Equation (21.5) states that fine cross-range resolutions and long wavelengths require large synthetic arrays. When D_{SAR} is comparable to the range R, the scene of interest is in the near-field with respect to the synthetic array (Chapter 9), giving rise to spherical wavefronts at the array and similarly challenging artifacts.

21.2.2 SAR as Range-Doppler Imaging

SAR is sometimes described in the context of range-Doppler imaging, often in manuscripts specializing in pulse-Doppler processing [e.g., 3]. As discussed in Chapter 17, the Doppler

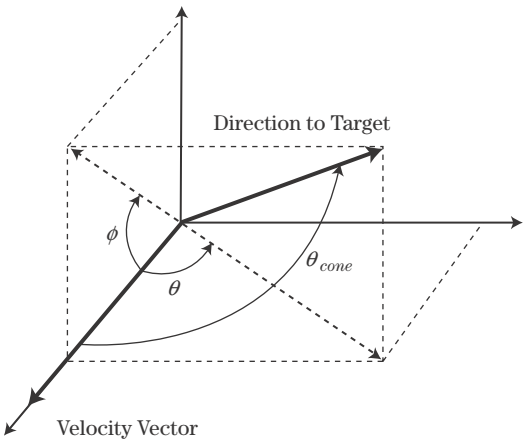

FIGURE 21-3 ■ Coordinate system showing azimuth, elevation, and cone angles, and vectors for platform velocity and direction to target.

frequency shift f_d generated by a stationary target at a radar moving at a speed v is

$$f_d = \frac{2v}{\lambda} \cos \theta_{cone} \tag{21.6}$$

where θ_{cone} is the *cone angle*, the angle between the radar velocity vector and the line-of-sight (LOS) vector from the radar to the target. The cone angle can be decomposed into azimuth θ and elevation ϕ angles defined with respect to the velocity vector

$$\cos \theta_{cone} = \cos \theta \cos \phi \tag{21.7}$$

Figure 21-3 contains a diagram of these angles.

Referencing azimuth and elevation to the velocity vector is consistent with nose-mounted forward-looking radar systems. As discussed in Section 21.2.1, imaging radars are often side-mounted and view a scene perpendicular to the velocity vector. Under these circumstances, azimuth is defined with respect to the side-looking direction, introducing a 90° shift in the azimuth coordinate system and thus causing the azimuth cosine in equation (21.7) to become a sine:

$$\cos \theta_{cone} = \sin \theta \cos \phi \tag{21.8}$$

Substituting (21.8) into (21.6) yields

$$f_d = \frac{2v}{\lambda} \sin \theta \cos \phi \tag{21.9}$$

Assuming a shallow elevation angle, (21.9) can be simplified to

$$f_d \approx \frac{2v}{\lambda} \sin \theta \tag{21.10}$$

Taking the partial derivative of (21.10) with respect to azimuth angle yields

$$\frac{\partial f_d}{\partial \theta} \approx \frac{2v}{\lambda} \cos \theta \tag{21.11}$$

and approximating ∂f_d and $\partial\theta$ with finite Doppler and azimuth extents Δf_d and $\Delta\theta$, respectively, gives

$$\Delta f_d \approx \left(\frac{2v}{\lambda}\cos\theta\right)\Delta\theta \tag{21.12}$$

Equation (21.12) relates azimuth extent to Doppler extent. In range-Doppler imaging the Doppler extent is set by Doppler filtering; specifically, the filter bandwidth B_d can be substituted for the Doppler width Δf_d in (21.12). Finally, equation (21.1) showed that an azimuth extent is related to a cross-range extent by the slant range. Making these substitutions into (21.12) gives

$$B_d \approx \left(\frac{2v}{\lambda}\cos\theta\right)\frac{\Delta CR}{R} \tag{21.13}$$

and rearranging the terms in (21.13) produces

$$\Delta CR \approx \frac{R\lambda}{2v\cos\theta}B_d \tag{21.14}$$

Equation (21.14) indicates that narrower Doppler filter bandwidths provide finer cross-range resolution. A simple approach to SAR imaging, then, is to apply the pulse history in each range bin to a Doppler filter bank, generated by a fast Fourier transform (FFT) for example, and to assign the output in each filter to a cross-range location in a manner consistent with equation (21.10).

As discussed in Chapter 17, the Doppler filter bandwidth B_d is inversely proportional to the data collection time, or *dwell time*, T_d. Applying this relationship to equation (21.14) yields

$$\Delta CR \approx \frac{R\lambda}{2vT_d\cos\theta} \tag{21.15}$$

The product of the platform velocity v and dwell time T_d is the data collection distance, equivalent to the SAR baseline D_{SAR} discussed in Section 21.2. Using $D_{SAR} = vT_d$, equation (21.15) becomes

$$\Delta CR \approx \frac{R\lambda}{2D_{SAR}\cos\theta} \tag{21.16}$$

Note that equation (21.16), developed using the Doppler framework, is equivalent to equation (21.5), which was formulated with the large antenna paradigm, when imaging broadside to the velocity vector ($\theta = 0$).

Like the large-aperture model, the Doppler model becomes cumbersome at low frequencies and fine resolutions. From equations (21.14), small cross-range resolutions at long wavelengths require narrow Doppler bandwidths, which in turn require long dwell times. Over long dwells platform motion causes the apparent scatterer locations to drift, so that returns move through multiple range and Doppler resolution cells. Severe migration over range and Doppler produces a badly blurred range-Doppler rendering of the scene. Consequently, range-Doppler imaging is appropriate for coarse resolutions at high carrier frequencies only.

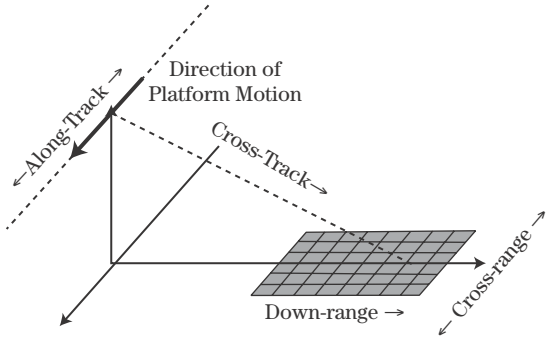

FIGURE 21-4 ■ Location in a SAR image is usually defined as a function of along-track and cross-track coordinates, or down-range and cross-range coordinates. For side-looking collections these coordinate systems are nearly equivalent.

21.2.3 SAR as a Signal Processing Exercise

Modern signal processing provides a very general and versatile framework for understanding SAR concepts and operation [4–6]. Indeed, the SAR discipline has benefited immensely from algorithms developed in related synthetic imaging disciplines. For example, two widely employed SAR image formation techniques were derived from principles first developed in the medical [7] and seismic imaging fields [8]. Moreover, signal processing accommodates SAR models and image formation methods developed using "inverse problem" approaches and constrained optimization algorithms [9].

From the signal processing point of view, SAR is just one example of a family of procedures that exploit sound, x-rays, positron emission, and other propagating energy sources for synthetic imaging. In general, image synthesis is a two-step procedure moving among three domains:

1. The object space, defined by the properties of the scene of interest.
2. The data space, comprising the raw radar measurements.
3. The image space, the final synthetic image.

In this development, all three spaces will be restricted to just two dimensions for simplicity. Hence, the SAR object space is the complex reflectivity of the scene versus down-range and cross-range location, the data are the complex returns recorded as a function of platform along-track location and "fast time" (range-delay time), and the final image is made up of complex pixels arrayed over down-range and cross-range.

The geometry shown in Figure 21-4 highlights the along-track, down-range, and cross-range dimensions. Note the additional term "cross-track," which is defined as range perpendicular to the platform direction of travel. For clarification, data "fast time" refers to the time delay into the measured record on each transmitted pulse and is equal to slant range divided by one-half the propagation speed. Analogously, the term "slow time" is sometimes used to refer to time over multiple pulses.[1]

[1]Of course, there is only one universal "time" for SAR data acquisition and processing. "Fast time" is reserved for rapid range-varying responses within the current time between transmitted pulses, so the start time of the transmission of each pulse is usually set to zero. "Slow time" is meant to describe changes over the dwell time, over many pulses, with a slow time of zero referenced to either the start or midpoint of the collection.

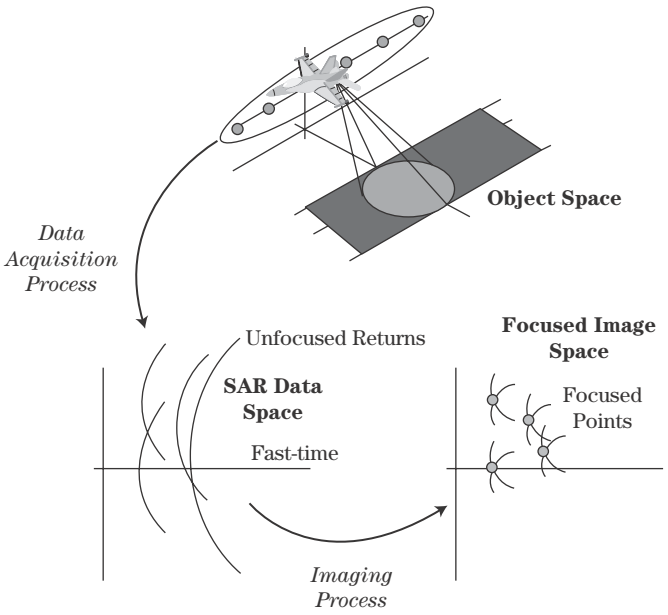

FIGURE 21-5 ■ The SAR process involves three spaces and two transformations. Data acquisition provides the transformation from scene reflectivity to raw data, while image formation operates on the raw data to yield the final SAR image.

From the point of view of the signal processing paradigm, the two steps of SAR imaging are as follows:

1. **Data acquisition:** Measurement of the response of the scene of interest over a range of frequencies and angles. The resolution obtainable in the final image depends on the frequency and angle parameters. This step is the transformation of the scene from object space to data space.
2. **Image formation:** Matched filtering of the measured data to the predicted responses from the scene of interest. This step is the transformation from the measured data to the final synthetic image. Image formation can be accomplished with any of a large number of algorithms, all of them exact implementations of, or approximations to, filtering matched to point target responses.

Figure 21-5 depicts these domains and transformations for SAR.

21.3 | RESOLUTION RELATIONSHIPS AND SAMPLING REQUIREMENTS

While many metrics are available to describe SAR image quality, the most important figure of merit in many applications is "resolution." *Resolution*, specifically spatial resolution, has units of distance (e.g., meters, inches) and is the limit on the ability to resolve, or to distinguish between, two closely spaced point scatterers. In essence, fine ("high") resolution means scatterers placed in proximity will appear as distinct returns in the final image. As SAR images are two-dimensional, a resolution value applies to each dimension.

In SAR imagery having coarse resolution, say tens or hundreds of meters, first-order terrain types (e.g., water, forest, urban) may be discerned by measuring pixel intensity and image texture. At finer resolutions, on the order of several meters, stands of trees, individual vehicles and buildings, and cultural features like roads and railways can be

perceived. At 1 meter of resolution, individual trees are visible, and the size, shape, and orientation of buildings and vehicles are apparent. At a small fraction of a meter, SAR images render much like photographs; small objects like signs and lampposts can be detected and vehicles identified by type.

The wealth of information available in a submeter resolution image makes fine resolutions highly attractive, ignoring for the moment demands on hardware, processing, and data storage. But how are these resolutions achieved? Fundamentally, they require the scene of interest be measured over a wide range of angles and frequencies. To justify this assertion, consider the following thought experiment.

Imagine a stationary radar recording the return from a scene using a single-frequency waveform, that is, a pure continuous wave (CW) tone. All of the scatterers in the scene will interfere with one another and produce a single complex return at the radar output, one in-phase (I) and quadrature (Q) (or, equivalently, one amplitude and phase) value. The "resolution" of this system is very poor, equal to the size of the illuminated scene.

If the radar changes frequency, the scene scatterers will constructively and destructively interfere in a different way, yielding a different I and Q value. By measuring the scene over several discrete frequencies, a number of different complex measurements are produced. Chapter 14 discusses the Fourier relationship between frequency and time, which allows measurements collected over a frequency bandwidth to be used to resolve returns into range bins. In summary, measurements in frequency provide down-range resolution.

Similarly, if the radar is moved to a new location, the differential ranges from the radar to all the scatterers change, causing their returns to constructively and destructively interfere in an altered way, thus producing a modified I and Q value. Differential range changes most rapidly when the radar is moved not toward or away from the illuminated scene but rather over angle across the LOS to the scene. Movement over angle generates variations in the complex measurements even when the CW frequency is fixed. Chapter 17 notes the Fourier relationship between angular motion and azimuth location, which allows measurements over angle to be used to resolve and bin returns into cross-range. In summary, measurements over angle provide cross-range resolution.

21.3.1 Resolution Relationships

The range resolution Δ of any imaging system is equal to the ratio of the propagation speed c of the imaging energy through the supporting medium and the bandwidth B of the measurements

$$\Delta = \frac{c}{B} \tag{21.17}$$

where resolution is in units of distance. While there exist many formulae for resolution, (21.17) is consistent with the classical Rayleigh criterion for resolution, which states that two scatterers are resolved when the peak response from one falls at or outside the first null in the response from the other.

Imaging methods that employ two-way propagation, such as radar, realize a factor-of-two gain in resolution:

$$\Delta = \frac{c}{2B} \tag{21.18}$$

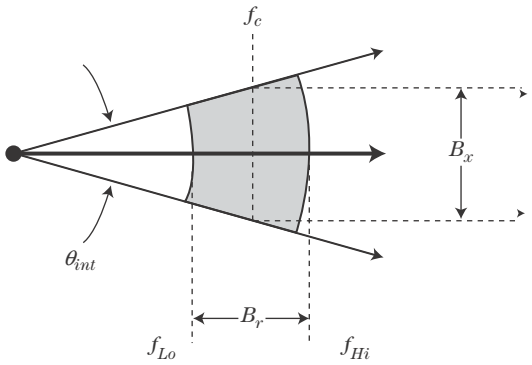

FIGURE 21-6 ■ Data support for a SAR collection is two dimensional and is a function of the waveform frequencies and integration angle. These quantities may be depicted in a polar coordinate system.

In SAR, the down-range resolution Δ_{DR} is given by equation (21.18) with RF bandwidth B_r provided by the frequency support of the radar waveform

$$\Delta R = \frac{c}{2B_r} \tag{21.19}$$

The cross-range resolution expression for SAR can be derived from (21.18) by referring to Figure 21-6, which depicts the angle-frequency support of measurements made with respect to the scene of interest. This information appears in a polar plot with waveform frequency and bandwidth along the radials and measurement azimuth over angle. Measurements are collected over an RF bandwidth B_r centered about a carrier frequency f_c, yielding low and high frequencies f_{Lo} and f_{Hi}. Measurements are also collected over a so-called *integration angle* θ_{int} defined by the upper and lower radials. Integration angle is the angular extent over which the SAR system collects returns from the scene of interest, as defined by the bearing angle from scene center to the radar.

Define a "cross-range bandwidth" B_x, perpendicular to the RF bandwidth B_r, as shown in the figure. This bandwidth is, for small integration angles, equal to the product of the carrier frequency f_c and integration angle θ_{int}

$$B_x \approx f_c \theta_{int} \tag{21.20}$$

Substituting for bandwidth in the resolution expression (21.18) with the cross-range bandwidth gives a formula for cross-range resolution ΔCR

$$\Delta CR = \frac{c}{2B_x} = \frac{c}{2f_c\theta_{int}} \tag{21.21}$$

Rewriting (21.21) in terms of the wavelength of the RF carrier λ_c gives

$$\Delta CR = \frac{\lambda_c}{2\theta_{int}} \tag{21.22}$$

Equation (21.22) is consistent with the expressions for cross-range resolution derived under the antenna (21.5) and Doppler (21.16) SAR paradigms, as integration angle is approximately equal to the ratio of the SAR aperture length D_{SAR} and the range to the center of the scene R:

$$\theta_{int} \approx \frac{D_{SAR}}{R} \tag{21.23}$$

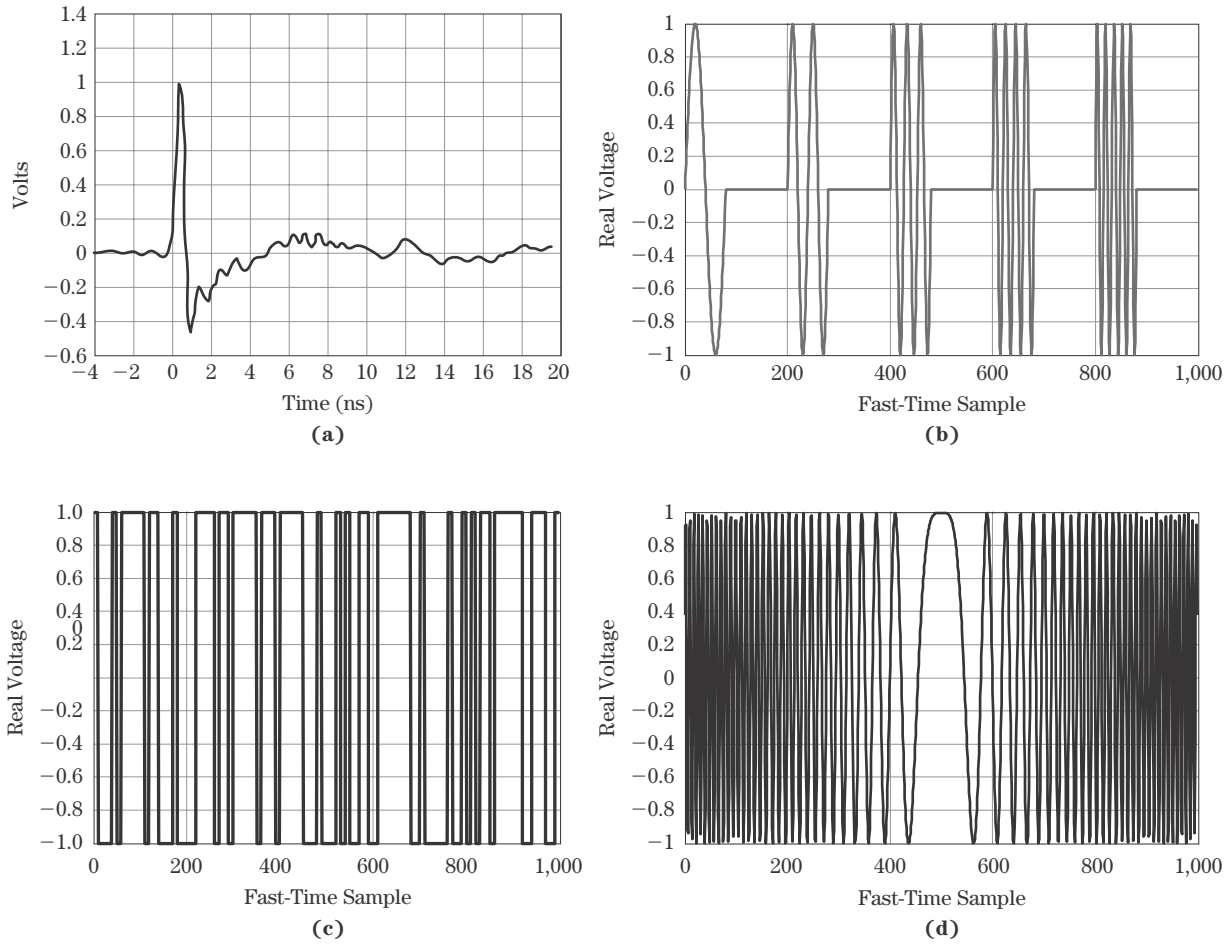

FIGURE 21-7 ■ Four options for wideband waveforms are (a) a short-time pulse, (b) a stepped-frequency series of pulses, (c) a bi-phase modulated pulse, or (d) a linear FM pulse.

Together, equations (21.19) and (21.22) support the earlier assertion that fine resolutions require measurement over frequency (wide waveform bandwidths) and angle (large integration angles). Additionally, equation (21.22) suggests that fine cross-range resolutions are easier to achieve at short wavelengths.

Figure 21-7 depicts the various waveforms a radar may use to collect measurements over a wide range of frequencies; these are described in more detail in Chapter 20. A short-duration transmit pulse, shown in Figure 21-7a, is arguably the clearest path to generating wide bandwidths and fine range resolutions. A narrow pulse obviously permits scene returns to be partitioned into very fine range bins. Due to the Fourier relationship between time and frequency, the record from a short-time pulse also provides measurements of the scene over a wide bandwidth. Thus, the fine resolution of the short pulse is consistent with the large bandwidth needed for fine resolution as seen in equation (21.19). However, short pulses tend to be energy limited and are therefore appropriate for short-range applications only.

Figure 21-7b shows a stylized representation of one solution to the energy limitations in a short-time pulse. The stepped frequency waveform consists of a series of pulses, each at a slightly different narrowband frequency. Every pulse is of long duration, sufficient

to effectively immerse the entire scene of interest, thereby measuring its response at one pure frequency. The stepped-frequency radar transmits and receives one pulse at a time, collecting a single I and Q value at each frequency. The stepped-frequency waveform, then, explicitly measures the response of a scene over a wide bandwidth, one discrete frequency at a time. By Fourier transforming over the frequency measurements the radar data processor can synthesize the same fine-resolution range profile provided by a short-duration pulse of equivalent bandwidth. Moreover, the use of multiple long pulses means the stepped frequency waveform is not subject to energy limitations. However, it takes significant time to collect stepped-frequency measurements over a wide bandwidth, so this waveform is not appropriate for dynamic environments. While stepped frequency waveforms are common in carefully controlled antenna and radar cross section (RCS) measurement activities, they are rarely employed by moving platforms.

Phase or frequency modulation of a single long-duration pulse is a common solution to the competing requirements of wide bandwidths, high energy, and operation in dynamic environments. Figure 21-7c shows an example of a biphase modulated pulse. Phase modulation is commonly used in radars having moderate bandwidths, though application in wideband systems has been limited until recently due to the requirement for high-speed analog-to-digital conversion (ADC) and computationally intensive matched filtering. Existing SAR systems use frequency modulation, specifically linear frequency modulation (LFM), also known as a "chirp" waveform, almost exclusively (see Chapter 20). An example of the baseband representation of an LFM pulse appears in Figure 21-7d. The linear chirp waveform provides wide bandwidth over a long pulse having appreciable energy. In addition, LFM is the only modulation appropriate for so-called *dechirp-on-receive* or *stretch processing*, a computationally efficient matched filtering procedure for pulse compression that also tolerates low to moderate ADC rates. Finally, LFM waveforms are Doppler-tolerant, permitting high-speed platforms like satellites in low Earth orbit to accomplish SAR imaging without the added complication of a bank of Doppler-dependent matched filters.

In SAR, integration angle is provided by the relative motion between the radar platform and the scene of interest. Examples appear in Figure 21-8. In a *stripmap* SAR collection, shown in Figure 21-8a, the platform moves along a nominal straight-line path, with the radar antenna oriented off to one side and perpendicular to the flight path. As the platform moves, targets, clutter, and other scatterers move through the antenna mainbeam, and the effective bearing angle of the radar to these returns varies. The radar collects along a contiguous swath parallel to the radar direction of motion.

In a *spotlight* collection, shown in Figure 21-8b, the platform maintains a straight-line path, but the radar antenna is pointed toward a scene of interest. Beam-pointing may be accomplished by mechanical panning of a gimbaled antenna or, if the antenna is an

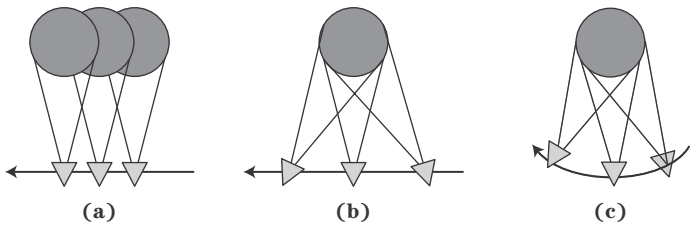

FIGURE 21-8 ■ Three collection options for achieving integration angle are (a) stripmap, (b) spotlight with mechanical or electronic steering of the real antenna beam onto a scene of interest, or (c) spotlight realized by flying a circle about the scene of interest.

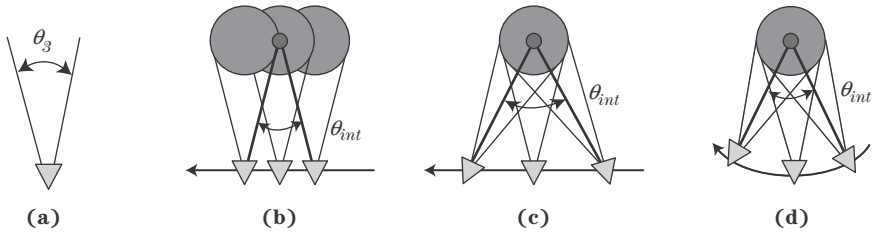

FIGURE 21-9 ■ Given the beamwidth of a real antenna (a), the stripmap integration angle (b) is limited by the real beamwidth, while spotlighting with linear (c) or circular (d) flight paths can realize integration angles greatly exceeding the real antenna beamwidth.

electronically scanned array (ESA), via analog beam steering. By aiming the beam at particular point as the platform flies past, the radar can collect data for that point over a longer time than in the fixed-beam stripmap mode. The extended dwell time afforded by beam-pointing increases the integration angle for scatterers in the scene of interest and so improves cross-range resolution. A drawback of spotlight operation is that longer acquisitions on scenes of interest come at the expense of returns from other regions along the flight path. That is, stripmap yields a moderate resolution image that is continuous along the flight path, whereas spotlight generates fine-resolution images intermittently, with gaps in coverage along the platform's ground track. Finally, a spotlight collection can be achieved by flying a curved path about a scene of interest, as shown in Figure 21-8c, so that beam-pointing is accomplished by the motion of the platform. If the path is circular, a full 360° of integration angle can be garnered against scatterers in the scene.

Figure 21-9 summarizes the integration angles provided by the various collection schemes. Figure 21-9a shows a physical antenna with a real beamwidth θ_3. In the stripmap collection shown in Figure 21-9b, measurements are collected against scatterers within the imaged swath only while they fall within the beamwidth θ_3 of the transmit/receive antenna. Simple geometry indicates the maximum stripmap integration angle is equal to the antenna beamwidth. From the resolution relation in equation (21.22) and setting $\theta_{int} \leq \theta_3$,

$$\Delta CR \text{ (stripmap)} \geq \frac{\lambda_c}{2\theta_3} \tag{21.24}$$

Achievable stripmap cross-range resolution is bound by the real antenna beamwidth: wider beamwidths provide increased integration angles and finer resolutions. On the other hand, the spotlight modes in Figures 21-9c and 21-9d clearly allow the integration angle to far exceed the antenna beamwidth and are therefore capable of much finer cross-range resolutions.

At this point it is convenient to highlight a nuance in the stripmap and spotlight terminology. Note that linear motion is common to the stripmap and the first spotlight methods shown in Figure 21-8. A linear collection geometry results in a specific scatterer response in the raw radar data, regardless of whether the real beam was steered. SAR image formation algorithms are designed based on the expected response of scatterers in the raw data. Thus, algorithms geared toward linear collections, sometimes called stripmap techniques, are equally applicable to both stripmap and linear spotlight collections. In contrast, the circular spotlight collection shown in Figure 21-8c gives rise to a very different scatterer signal history. Several imaging methods, sometimes referred to as spotlight techniques, are

tailored toward data collected in a circular fashion (or data preprocessed, through digital delays and interpolation, to appear as though they were collected from a circular path). Thus, when employing the terms stripmap and spotlight, care must be taken in stating whether the appellation applies to the means of generating integration angle or to the image formation technique.

21.3.2 Synthetic Aperture Sampling Requirements

In the course of collecting SAR data a number of sampling requirements must be met lest aliased returns degrade the final SAR image. Time and frequency sampling is covered in Chapter 14; here the discussion will be restricted to requirements for sampling along the SAR collection path.

The diagram in Figure 21-10a contains an antenna with beamwidth θ_3 looking off to the right. The antenna platform is moving from bottom to top; equivalently, scatterers in the imaged swath move from top to bottom through the antenna mainbeam. Two scatterers are shown: the upper one moving into the top edge of the mainbeam, and the lower one moving out of the mainbeam.

As discussed in the previous section, SAR waveforms are typically pulsed; CW SAR systems are quite rare. Pulsed waveforms are required for monostatic antenna implementations and, through judicious time gating, allow returns to be constrained to the down-range swath of interest. Transmission and reception of pulses means the response of the illuminated scene is recorded at discrete, uniformly spaced locations along the radar flight path. Radar movement between two pulses causes a range decrease to scatterers along the leading edge of the antenna beam, as shown in Figure 21-10b. This range decrease is a function of the distance between sample points d and the angle to the scatter, which is equal to half the beamwidth. From the right triangle construction in Figure 21-10c, the far-field range decrease dR is

$$dR = d \sin\left(\frac{\theta_3}{2}\right) \tag{21.25}$$

Due to symmetry about the mainbeam direction, the distance to the receding scatterers increases by the same amount.

It has already been noted that SAR is a coherent collection and imaging process, requiring measurement of RF phase. The phase change on the leading edge scatter due to the motion of the platform in Figure 21-10b depends on the range change normalized by

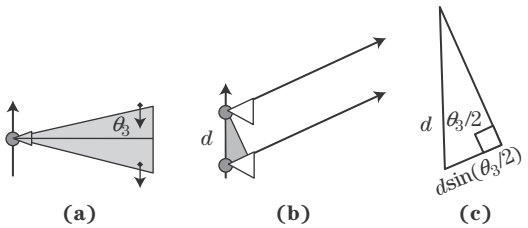

FIGURE 21-10 ■ Geometry for deriving the along-track sampling requirements for stripmap mode, (a) platform moving from bottom to top with antenna pointed to the right, (b) distance between along-track sample points d, and (c) differential range change to a scatterer on the leading edge of the mainbeam.

the RF wavelength. This phase decrease $\Delta\psi$ in radians is

$$\Delta\psi = 2\pi \left(2\frac{dR}{\lambda}\right) \tag{21.26}$$

The factor of 2 inside the parentheses appears because both the transmit and receive positions move with the radar, so the effective two-way range change is twice dR.

Combining (21.25) and (21.26) yields

$$\Delta\psi = 2\pi \left[2\frac{d}{\lambda}\sin\left(\frac{\theta_3}{2}\right)\right] \tag{21.27}$$

A coherent radar system is incapable of unambiguously measuring phase changes greater than 180°. A phase decrease of 179° is unique, but a decrease of 181° looks the same as an increase of 179°. Because the scatterers on the leading and trailing edges of the beam give rise to equal but opposite phase changes, the phase change to either side must not exceed 180°, or π radians:

$$|\Delta\psi| = \left|2\pi \left[2\frac{d}{\lambda}\sin\left(\frac{\theta_3}{2}\right)\right]\right| < \pi \tag{21.28}$$

Phase ambiguity is avoided by sampling along the flight path at sufficiently frequent intervals. From (21.28),

$$d < \frac{\lambda}{4\sin\left(\frac{\theta_3}{2}\right)} \tag{21.29}$$

As the value of an angle is always larger than the sine of that angle ($\sin\theta < \theta$), the bound in equation (21.29) can be simplified to

$$d < \frac{\lambda}{2\theta_3} \tag{21.30}$$

Equation (21.30) states that wider real beamwidths require finer sampling along the collection track. The sampling interval in (21.30) is set not by the wavelength at the carrier frequency but by the shortest wavelength λ_{min} of the waveform bandwidth

$$d < \frac{\lambda_{min}}{2\theta_3} \tag{21.31}$$

The consequences of violating the along-track sampling limit in equation (21.31) depend on the image formation technique and final image resolution. At coarse resolutions, undersampling is manifested primarily as a wrapping of returns in cross-range; that is, returns from a scatterer at a positive cross-range location beyond the limit of the final image will be aliased back into the image at a negative cross-range. At fine resolutions aliased returns tend to defocus and increase the effective noise level across the entire image. To preclude these degradations entirely it is prudent to use a more pessimistic value for beamwidth in equation (21.31), such as the null-to-null beamwidth $2\theta_R$, where θ_R is the peak-to-null (Rayleigh) beamwidth. Then, (21.31) becomes

$$d < \frac{\lambda_{min}}{2\,(2\theta_R)} \tag{21.32}$$

Antenna null-to-null beamwidths are typically about twice as wide as the 3 dB beamwidths θ_3 commonly used in resolution calculations.

The relationship in equations (21.32) was derived from a stripmap point of view as shown in Figure 21-10 but tends to hold for the circular spotlight collection geometry in Figure 21-8c as well. Sampling requirements for linear spotlight and squinted stripmap (with the antenna beam fixed away from broadside) are more complicated and depend strongly on the particular image formation technique applied to the data.

21.3.3 Miscellaneous Relationships

The formulae for resolution and sampling can be combined in various ways to derive constraints on SAR operations. For example, for square resolution cells the down-range and cross-range resolutions in equations (21.19) and (21.22) are equal, yielding

$$\frac{c}{2B_r} = \frac{\lambda_c}{2\theta_{int}} \tag{21.33}$$

Rearranging and replacing carrier wavelength with carrier frequency yields

$$B_r = f_c\theta_{int} \tag{21.34}$$

The right side of equation (21.34) is the "cross-range bandwidth" B_x in (21.20), so, not surprisingly, the RF and cross-range bandwidths must be equal for square resolution cells.

The null-to-null beamwidth of an antenna is a function of the physical size (length or diameter) D of the antenna and operating wavelength. A good rule of thumb for the peak-to-null beamwidth is

$$\theta_R \approx \frac{\lambda}{D} \tag{21.35}$$

when illumination is accomplished without amplitude tapering. (See Chapter 9 for more exact expressions for beamwidths and a discussion of the effects of tapering.) Using the minimum wavelength in equation (21.35) and inserting it into (21.32) gives an interesting relationship between along-track sampling and antenna size:

$$d < \frac{D}{4} \tag{21.36}$$

Equation (21.36) states that the radar must transmit and receive frequently enough to collect four pulses as the platform moves a distance equal to the antenna diameter.[2] Note the lack of dependence of the sampling requirement on wavelength/frequency: shorter wavelengths increase the phase sensitivity to range (21.26) but also decrease the antenna beamwidth (21.27) (for a fixed antenna size) at the same rate, producing a wash in the along-track sampling requirement.

A similar relationship for stripmap resolution can be developed with an approximate expression for antenna 3 dB beamwidth at the carrier frequency:

$$\theta_3 \approx \frac{\lambda_c}{D} \tag{21.37}$$

[2]The null-to-null beamwidth results in the factor of four. Some texts report a factor of two because they employ a less stringent beamwidth.

Combining (21.37) with (21.24) gives

$$\Delta CR \text{ (stripmap)} \approx \frac{D}{2} \tag{21.38}$$

Again, wavelength or frequency is absent this expression: higher frequencies result in narrower beamwidths for a given antenna size and therefore decreased integration angle, but wavelength decreases at the same rate for a wash in cross-range resolution. Note that equation (21.38) provides a lower bound on resolution; images having spoiled (coarser) resolution may be generated from full-resolution data.

Finally, equations (21.36) and (21.38) can be combined to relate the resolution limit to sampling requirements:

$$d < \frac{\Delta CR}{2} \text{(stripmap)} \tag{21.39}$$

Equation (21.39) is a handy rule of thumb for the required sampling interval when the stripmap resolution capability of a SAR system is documented but the operating frequency or antenna size is unknown.

21.4 DATA COLLECTION

As previously discussed, SAR is a two-step process: (1) data collection; and (2) image formation. In this section the data collection step is described in more detail.

This chapter began by noting the similarities between SAR and optical images, and now it is instructive to explore the differences in SAR and optical data collection. For example, to photograph a large region of terrain, a camera might be placed high overhead, as depicted in Figure 21-11. This geometry is common for aerial photogrammetry (map-making) and satellite photo-reconnaissance purposes and serves to minimize distortion of the scene in the final image. However, this geometry is completely unsuitable for radar imaging, as returns from the entire illuminated ground region would fall into a handful of range bins. By placing the radar off to the side, as shown in Figure 21-11, returns across the illuminated area can be subresolved into a large number of range bins. Imagining

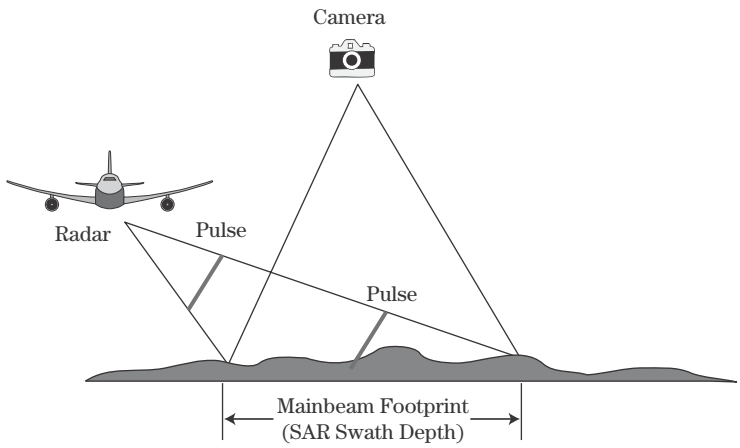

FIGURE 21-11 ■ Geometry of overhead photography of a scene of interest as compared to a typical SAR collection.

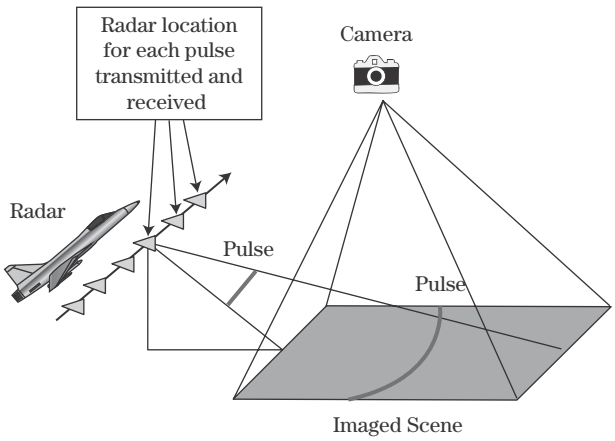

FIGURE 21-12 ■ The camera generates a 2-D image in one take, whereas the radar must collect data pulse-by-pulse over a long dwell.

for a moment the radar transmits a short-duration pulse, it can be seen that the outbound pulse will sweep across the SAR swath, allowing returns to be binned in time to form a high-resolution range profile.

In summary, optical imaging calls for steep look-down angles, generally 70° to 90°, whereas SAR imaging is typically accomplished at grazing angles of 10° to 45°. Images formed at steeper look-down angles suffer from dilation of the effective range resolution on the ground. (Resolution on the ground equals the resolution of the waveform divided by the cosine of the grazing angle; see Chapter 2.) Grazing angles shallower than 10° are theoretically acceptable. However, the radar not only receives returns but also provides the scene illumination. Real terrain tends to undulate mildly or is covered by high vegetation such as trees or bushes. Both phenomena cause large portions of the swath to be shadowed at extremely low grazing angles. (See Chapter 5 for a discussion of clutter shadowing effects.) For this reason SAR collection geometries are usually set to ensure grazing angles of at least 10°.

Figure 21-12 helps to clarify another important difference between optical and SAR imaging. A camera observes the entire scene through a two-dimensional recording medium (a chemical film emulsion or an electronic focal plane array) at the image focal plane and therefore requires just a fraction of a second to collect a data "snapshot" and form an image. At any given location the radar also views the entire scene; however, scatterers at the same slant range fall into a single range bin, so the radar's "snapshot" is a one-dimensional range profile. SAR image formation requires data over many pulses, each collected from a different location. These changing locations provide the integration angle required to achieve cross-range resolution. However, it does take some time for the platform to move and collect all of the measured data. For coarse resolutions this may be only a fraction of a second. Fine resolutions require large integration angles that, at long slant ranges, entail long SAR data collection distances. A slow-moving platform may require many seconds, even several minutes, to traverse the synthetic aperture and collect sufficient data for image formation.

Figure 21-13 further expands on the details behind a SAR data collection. In contrast to real-beam mapping systems such as SLAR wherein a very narrow antenna beam is used to resolve scatterers in cross-range, the SAR beamwidth is wide enough to illuminate the entire scene of interest and does so over many pulses. Each pulse transmission and reception position produces a one-dimensional stream of I and Q values.

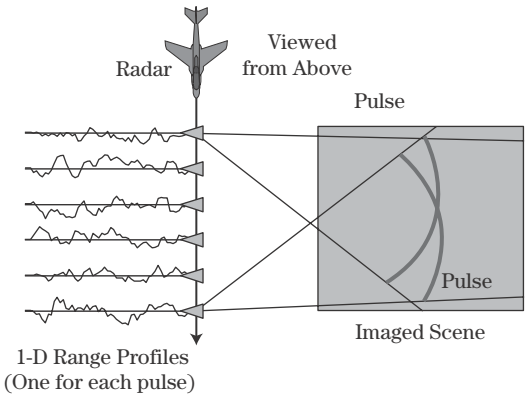

FIGURE 21-13 ■ Every pulse illuminates the entire scene of interest and produces a 1-D, complex range profile.

Figure 21-13 is also convenient to introduce a common simplification in the development of SAR collection geometries, the so-called *stop-and-hop model*. In reality the radar is moving continuously, and the radar location changes slightly in the time it takes for a pulse to propagate out to the scene and back. Hence, transmit and receive locations are not quite the same; the collection is bistatic, in the strictest sense. However, this displacement between transmit and receive location is usually very small compared with the range to the image scene and so may be neglected. From the signal processing point of view (e.g., sampling requirements, generation of matched filters for imaging), it can be assumed that the transmit and receive positions are colocated. In this model, the radar stops at one location, transmits and receives a pulse, then hops to the next location. The "virtual" collection point is usually chosen to be at the bisector between the transmit and receive positions.

The stop-and-hop model allows complicated two-way geometric calculations to be simplified to a one-way expression and a multiplicative factor of two for two-way propagation. It is appropriate when the transmit/receive displacement is very small compared with the imaging range, which is equivalent to restricting the platform speed to be much slower than the pulse propagation speed. This is always the case in radar, even for space-based collections where the platform speed can be several kilometers per second, but the stop-and-hop model may not be appropriate for some kinds of acoustic imaging, like ship-based sonar.

Finally, it is useful to justify the importance of phase information to SAR imaging. SAR is a coherent process and requires recording of both amplitude and phase. Recall that the entire scene is illuminated over the course of the SAR collection. For that reason the complex value recorded in any given range bin reflects the coherent accumulation of the returns from many scatterers distributed across the swath at that particular range. As the platform moves, the scatterers interfere constructively and destructively in different ways, causing amplitude and phase fluctuations over time. Therefore, the signal history bears no resemblance to the actual distribution of scatterers in the bin but contains the information the SAR image processor needs to separate those returns in cross-range in the final image.

In a way, coherent radar has two means to measure the range to a target. The first is relatively coarse and involves either measuring time delays on pulse returns or forming range responses using the frequency content in a modulated pulse. The fundamental product is the same: A one-dimensional profile consisting of range bins possessing a resolution on the order of many meters, several feet, or just a few inches. The profile allows

the absolute range to a target to be measured to within a fraction of the range resolution. Thus, pulse timing and waveform modulation provides gross resolution and location of targets in down-range.

The second range estimate originates from phase information, which provides a very fine but highly ambiguous measure of range. Interestingly, these properties are exploited to isolate returns not in down-range but rather cross-range. Recall that one cycle of phase shift corresponds to a change in two-way distance equal to half the wavelength (for two-way collections). Radar wavelengths are almost always much smaller than range bin size, so phase provides a very accurate measure of range. Higher carrier frequencies afford more accuracy due to the smaller value of wavelength λ. For example, W-band systems operating at 94 GHz can use phase to measure range to within 3 mm. Unfortunately, this measurement is highly ambiguous, having an ambiguity interval equal to half a wavelength. For example, if an X-band radar having a wavelength of 3 cm measured a phase angle of 180°, the distance to the source scatterer would be (1.5 cm) $\times$ (180°/360°) = 0.75 cm plus an unknown integer number of half-wavelengths. The scatterer might be only 0.75 cm from the phase center of the radar antenna, or it could be 0.75 cm plus 1 million intervening half-wavelengths (1,500,000.75 cm = 15.0000075 km) from the phase center.

The ambiguous nature of the phase measurement makes absolute phase values meaningless in all but the most near-field synthetic imaging applications. Instead, the progression of phase as the location of the radar varies is the principal concern. The phase trend observed from pulse to pulse is a function of the cross-range location of a target, as seen in Figure 21-14. In the diagram at the top, a single scatterer is located broadside to the SAR collection points. If the target is very far from the synthetic array, its return will fall into the same range bin for all pulses. Indeed, in the far field, the slant range to the scatterer changes so little that the radar will record about the same phase angle, 10° in the example. The lower diagram shows a scatterer just off the centerline. This displacement away from broadside cause the slant range from the radar to slightly decrease as it moves from top to bottom. The range variation is not sufficient to cause the scatterer's return to drift through

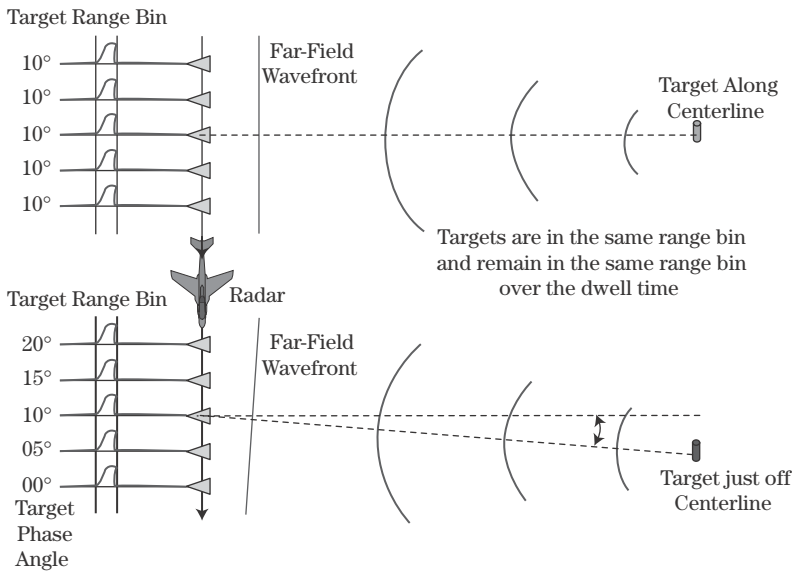

FIGURE 21-14 ■ Small changes in the cross-range location of a scatter cause a negligible change in the apparent range bin for that return but a significant change in the induced pulse-to-pulse phase progression for that return.

range bins (often referred to as *range migration*), but it is enough to generate a phase angle progression, 5° from pulse to pulse in this example. A scatterer removed still farther from broadside generates a larger phase change between radar positions, and a scatterer placed on the opposite side of the centerline causes a decreasing phase progression. Thus, phase history can be used to map returns to their appropriate cross-range locations. In summary, phase provides fine but highly ambiguous resolution and location of targets in range, but pulse-to-pulse phase progressions yield resolution and location in cross-range.

21.5 IMAGE FORMATION

Once raw radar data are acquired, image formation (i.e., the transformation from I and Q samples to the final SAR image) can be performed. There are a wide variety of image formation algorithms available that presume different collection geometries and make certain mathematical approximations, some very simple and suitable only for coarse resolution imaging, others more sophisticated and tailored to fine-resolution imaging, and some more computationally or memory efficient than others. All exploit the predicted return from a point source in the imaged scene. This *point spread response* (PSR) is the manifestation of an isotropic point scatterer in the raw data. In signal processing terminology, the PSR is the raw data "impulse response" of the SAR data acquisition system. Knowledge of the PSR is the key to designing an image formation algorithm to gather up the energy from a scatterer distributed throughout the raw data and focus it into a concentrated point-like return in the final SAR image.

In this section the PSR for a linear (stripmap) SAR collection geometry is derived and used to construct several image formation techniques.

21.5.1 SAR Coordinate Systems

Figure 21-15 revisits the domains and transformations introduced in Figure 21-5 but adds coordinate definitions. The top diagram shows the collection geometry; the location of

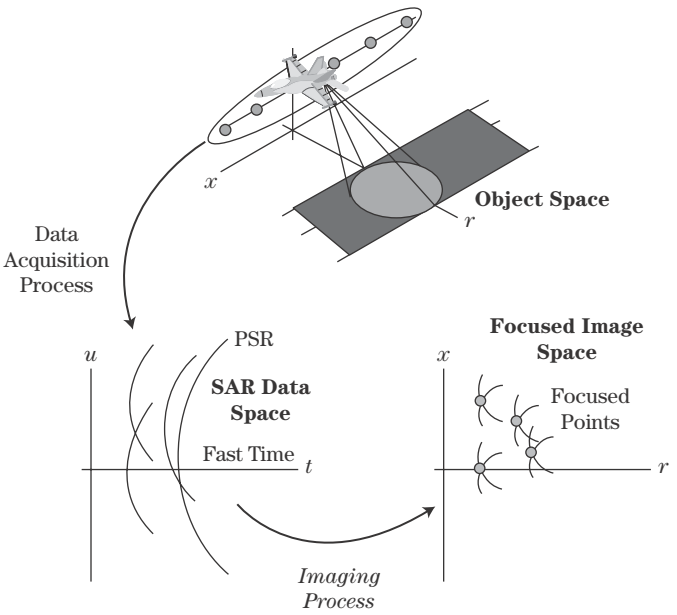

FIGURE 21-15 ■ The SAR process as depicted in Figure 21-5 with axes defined.

scatterers on the ground are determined by an along-track position x and cross-track range (distance from the platform flight line) r. The function $g(x, r)$ is the complex reflectivity of the imaged scene, including distributed natural clutter and man-made targets, as a function of along-track and cross-track location. Here $g(x, r)$ is modeled as a collection of isotropic point scatterers.

The second diagram in Figure 21-15 depicts the complex raw SAR data $d(u, t)$. This data is two-dimensional, with the vertical dimension showing the along-track location of the platform u where a given pulse was transmitted and received. In this development the scene coordinate x and data collection coordinate u are measurements of the same along-track position, but the former is dedicated to scatterer locations and the latter reserved for platform locations. The other dimension is the time delay t into the data on any given pulse. Here it is assumed that pulse compression has already been performed (see Chapter 20) if a long phase or frequency modulated pulse is used, so that t represents time into compressed range profiles.

The third diagram in Figure 21-15 shows the SAR image $f(x, r)$. The final image is formed to depict as accurately as possible the scene reflectivity, so the collection and image spaces share the same (x, r) coordinate system.

21.5.2 Linear Collection PSR

The PSR in the data $d(u, t)$ of a scatter located at (x, r) with reflectivity $g(x, r)$ is determined entirely by the slant range from the platform to the scatterer over the SAR data collection. The evolving slant range over the dwell allows the prediction of (1) amplitude variations due to geometric (R^4) loss, (2) any gross migration through compressed range bins, and (3) the fine pulse-to-pulse progression of carrier phase.

The platform is confined to the along-track axis and thus always has a zero cross-track component so that its location is $(u, 0)$. Using Figure 21-16 and the Pythagorean theorem, the slant range R to a scatterer at (x, r) from the platform at $(u, 0)$ is given by

$$R^2 = (u - x)^2 + r^2 \tag{21.40}$$

The slant range squared is simply the sum of the squared along-track range difference and the cross-track range to the scatterer. The hyperbolic form of equation (21.40) is commonly

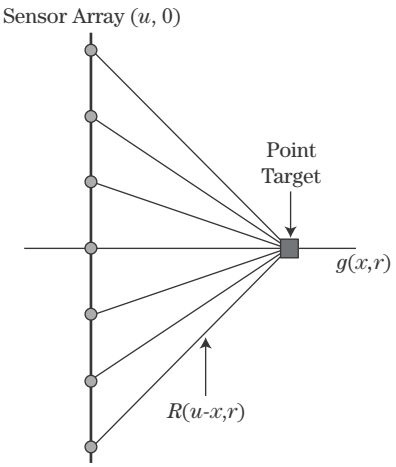

FIGURE 21-16 ■ Variation in slant range to a scatter at (x, r) due to platform motion.

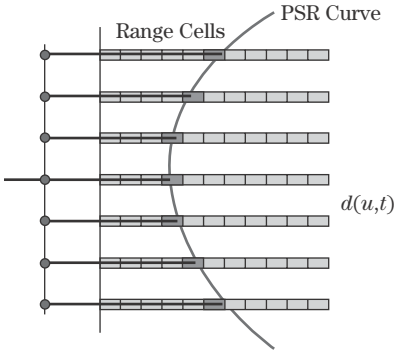

FIGURE 21-17 ■ The range variation to the scatterer over the dwell is described by the PSR. The PSR is manifested in the raw data as a hyperbolic migration of the return from a scatterer across compressed range bins.

associated with linear data collections. Writing the slant range explicitly as a function of the along-track difference and cross-track range gives

$$R(u;x,r) = \sqrt{(u-x)^2 + r^2} \tag{21.41}$$

The time delay t into the data for the return from a scatterer is then

$$\begin{aligned} t(u;x,r) &= \frac{2}{c} R(u;x,r) \\ &= \frac{2}{c}\sqrt{(u-x)^2 + r^2} \end{aligned} \tag{21.42}$$

The return from a point scatterer is concentrated in time at a delay given by equation (21.42). Figure 21-17 depicts the return from a point scatterer in the raw data, the PSR, over several pulse positions. Each pulse results in a range profile. The scatterer is manifested as a single strong return, highly concentrated in range, on any given pulse. Platform motion causes the range to the scatterer to change over the dwell yielding a time delay that takes the form of a hyperbola. The varying delay causes the return to migrate over time through range bins, first decreasing in time/range and then increasing. Because slant range determines measured phase angle, the hyperbolic time function also generates significant phase modulations (not shown in the figure) over the dwell.

It is useful to examine in more detail some properties of the PSR. From equation (21.42), the PSR of a scatterer at location (x_1, r) is nonzero at a time delay

$$t_1(u;x_1,r) = \frac{2}{c}\sqrt{(u-x_1)^2 + r^2} \tag{21.43}$$

The delay to the response from a second scatterer at the same cross-track range but displaced along-track by Δx to location $(x_1 + \Delta x, r)$ is

$$t_2(u;x_1+\Delta x,r) = \frac{2}{c}\sqrt{(u-(x_1+\Delta x))^2 + r^2} \tag{21.44}$$

Equation (21.44) can be rewritten as

$$t_2(u-\Delta x;x_1,r) = \frac{2}{c}\sqrt{((u-\Delta x)-x_1)^2 + r^2} \tag{21.45}$$

Defining a modified platform location $u' \equiv u - \Delta x$ for (21.45) yields

$$t_2(u'; x_1, r) = \frac{2}{c}\sqrt{(u' - x_1)^2 + r^2} \tag{21.46}$$

The PSRs for these two scatterers, given by equations (21.43) and (21.46), have the same hyperbolic form and differ only by a position shift in the u dimension. In general, all scatterers laying at the same cross-track range r give rise to PSRs with the same hyperbolic form but simply shifted in along-track location so that the PSR possesses *along-track invariance*. Therefore, a reference form for a given cross-track range can be derived from the PSR of a scatterer at an along-track location of zero ($x = 0$):

$$t_{REF}(u; r) = \frac{2}{c}\sqrt{u^2 + r^2} \tag{21.47}$$

Now perform a similar development for cross-track displacements. The PSR for a scatterer at $x = 0$ and r_1 is

$$t_1(u; r_1) = \frac{2}{c}\sqrt{u^2 + r_1^2} \tag{21.48}$$

and for a second scatterer displaced in cross-track range by Δr is

$$t_2(u; r_1 + \Delta r) = \frac{2}{c}\sqrt{u^2 + (r_1 + \Delta r)^2} \tag{21.49}$$

Unfortunately, the radical prevents expressing the cross-track range change as simply a time delay:

$$t_2(u; r_1 + \Delta r) \neq \frac{2}{c}\left(\sqrt{u^2 + r_1^2} + \Delta r\right) \tag{21.50}$$

From (21.50), the second PSR (21.49) is not simply the first PSR (21.48) delayed by a time consistent with the range change. The displacement in cross-track location actually changes the shape of the hyperbola, so the PSR exhibits *cross-track variance*. This effect is depicted in Figure 21-18. Four scatterers at the same along-track position and distributed in cross-track range produce hyperbolic PSRs centered at the same along-track position but delayed in time and having different shapes. The "bowing" of the hyperbola is more pronounced for scatterers close to the platform, and becomes shallower as cross-track

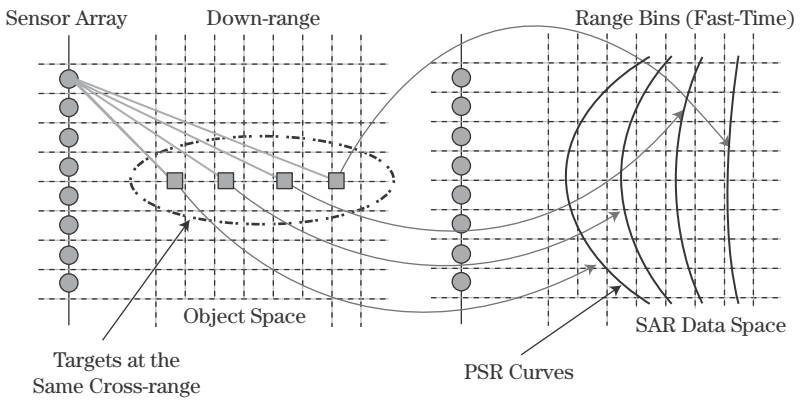

FIGURE 21-18 ■ Scatterers at different cross-track (down-range) locations have different PSR forms. Curvature decreases as range increases.

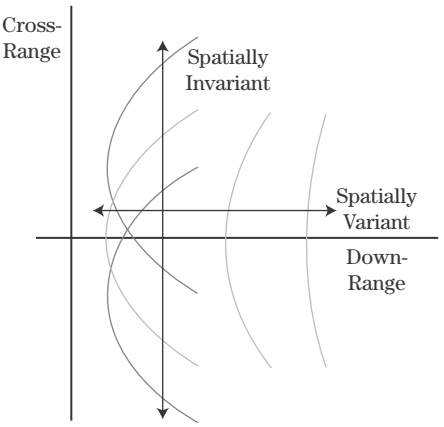

FIGURE 21-19 ■ Scatterers at different along-track (cross-range) location have the same PSR form, but with an along-track offset.

range increases. Mathematically, the PSR is spatially invariant along-track but spatially variant in the cross-track dimension.

Referring to Figure 21-19, the properties of the linear collection PSR can be summarized as follows:

1. The PSR is, in general, a two-dimensional (spatial and temporal) function in u and t.
2. The PSR is not separable in u and t (it cannot be constructed as the product of functions in u only and t only).
3. The PSR has a hyperbolic form that causes slant range to be dependent on the square root of platform and scatterer locations.
4. The PSR form varies with scatterer cross-track range.
5. The PSR form is the same for scatterers at the same cross-track range.

The first four properties complicate the image formation process, while the fifth provides structure an imaging algorithm can exploit, as shall be seen.

Knowledge of the PSR will now be used to derive *Doppler beam sharpening* (DBS), the oldest and most fundamental SAR image formation technique [10].

21.5.3 DBS Derivation

It is useful to begin with a qualitative presentation of DBS as a pulsed-Doppler imaging mode. Figure 21-20 depicts the platform moving from left to right with a side-looking radar pointed toward the top of the diagram. Range bins subdivide the illuminated scene in slant range. The Doppler frequency f_d in hertz from a scatterer is given by equation (21.6),

$$f_d = \frac{2v}{\lambda} \cos \theta_{cone}$$

where v is the platform ground speed, and θ_{cone} is the cone angle between the scatterer and the platform velocity vector. Azimuth angle θ is defined relative to the radar look direction. From Eq. (21.10)

$$f_d \approx \frac{2v}{\lambda} \sin \theta$$

Returns at different azimuth angles have different Doppler shifts. Because cross-range is a function of azimuth angle, Doppler filtering allows partitioning of the returns across the

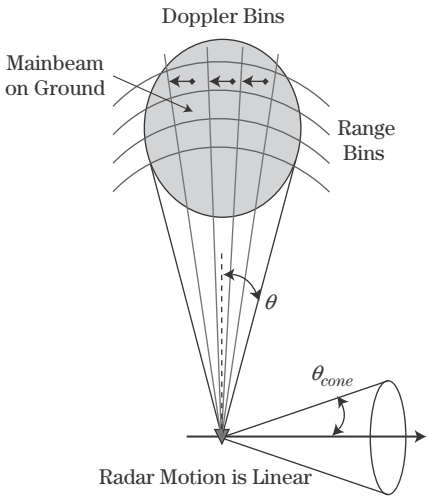

FIGURE 21-20 ■ Arranging ground returns as a function of slant range and Doppler yields a 2-D rendering of the scene of interest.

illuminated scene. DBS, then, uses range binning and Doppler filtering to create a range-Doppler map of the scene. The DBS image maps to slant range and cone angle but at long ranges and for small scene sizes closely approximates a rectilinear down-range-cross-range grid.

DBS is now examined from the PSR point of view. Figure 21-21 shows the hyperbolic PSRs of various scatterers in the range-compressed radar data. DBS assumes a relatively short collection time and coarse range resolution, so that any migration of the returns across range bins can be neglected. As shown in the figure, scatterer returns are then confined to a single range bin. This DBS approximation simplifies the first and second PSR properties from the previous section: the PSR is now a one-dimensional function confined to a single range bin. This greatly simplifies the task of the image former, which may now focus returns by operating on one range bin at a time.

The PSR in equation (21.42) can be rewritten as

$$\begin{aligned} t\,(u;x,r) &= \frac{2}{c}\sqrt{(u-x)^2+r^2} \\ &= \frac{2}{c}r\sqrt{1+\frac{(u-x)^2}{r^2}} \end{aligned} \tag{21.51}$$

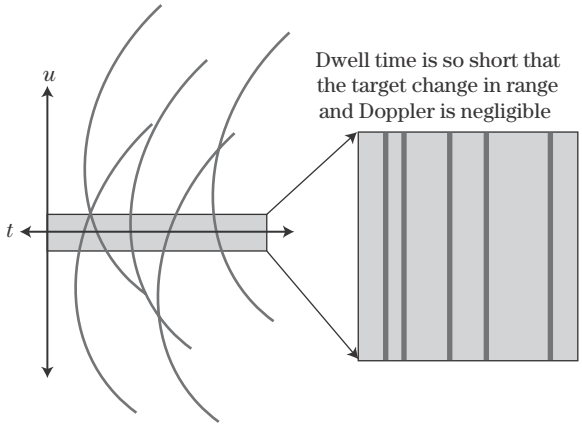

FIGURE 21-21 ■ For short collection times and coarse range bins each hyperbolic PSR is constrained to one range bin over the dwell.

The radical can be eliminated by performing a binomial expansion on its argument. The binomial expansion is simply the first two terms in a Taylor series expansion and is given as

$$(1+w)^p \approx 1 + pw, \quad w \ll 1 \tag{21.52}$$

Applying (21.52) with $p = 1/2$ to (21.51) gives

$$t(u;x,r) \approx \frac{2}{c} r \cdot \left(1 + \frac{(u-x)^2}{2r^2}\right), \quad (u-x) \ll r \tag{21.53}$$

In equation (21.53) it has been assumed that the along-track offset between the platform and the scatterer is much less than the cross-track range to the scatterer so that the condition of (21.52) is satisfied. Simplifying equation (21.53) yields

$$t(u;x,r) \approx \frac{2}{c}\left(r + \frac{(u-x)^2}{2r}\right) \tag{21.54}$$

Equation (21.54) is a quadratic approximation to the exact hyperbolic form of the PSR. The quadratic form changes the third PSR property to one more convenient for image formation.

Recall that DBS assumes that the slant range and time-delay variations are small enough that amplitude changes due to R^4 losses and migration through range bins can be neglected. Consequently, the primary manifestation of these range changes in the data is on the measured phase. Recall also that imaging relies not on absolute phase but on the phase progression as a function of platform location. Expanding equation (21.54),

$$t(u;x,r) \approx \frac{2}{c}\left(r + \frac{u^2}{2r} - \frac{ux}{r} + \frac{x^2}{2r}\right) \tag{21.55}$$

it is seen that the first and last term are functions of just the scatterer location (x, r). Only the second and third terms depend on the platform location u and so capture the time-delay changes over the collection. Reserving these terms to define a time-delay variation Δt as a function of u gives

$$\Delta t(u;x,r) \approx \frac{2}{c}\left(\frac{u^2}{2r} - \frac{ux}{r}\right) \tag{21.56}$$

The phase progression $\Delta\psi$ due to the time-delay variation of equation (21.56) is (in radians)

$$\begin{aligned} \Delta\psi &= 2\pi f_c \Delta t(u;x,r) \\ &\approx \frac{4\pi}{\lambda_c}\left(\frac{u^2}{2r} - \frac{ux}{r}\right) \end{aligned} \tag{21.57}$$

The first term does not depend on the along-track position of the scatterer. It is the *same* for all scatterers at a given cross-track range and serves to simply modulate the data by a quadratic phase function. If the center of a collection of length D_{SAR} is set to $u = 0$, then

the quadratic term

$$\Delta\psi_{QT} \equiv \frac{4\pi}{\lambda_c}\left(\frac{u^2}{2r}\right)$$

has a maximum value $\Delta\psi_{QT,MAX}$ at $\pm D_{SAR}/2$ equal to

$$\Delta\psi_{QT,MAX} = \frac{\pi D_{SAR}^2}{2r\lambda_c} \tag{21.58}$$

Quadratic phase error (QPE) effects on imagery are generally negligible if the maximum angular deviation is much less a than a phase cycle. A commonly enforced limit is $\pi/2$:

$$\Delta\psi_{QT,MAX} < \frac{\pi}{2}$$

When combined with equation (21.58), this gives a synthetic aperture limit of

$$D_{SAR} < \sqrt{r\lambda_c} \tag{21.59}$$

Baseline DBS imaging employs geometries that meet this constraint and so allow the first term in equation (21.57) to be omitted, so that

$$\Delta\psi \approx -\frac{4\pi}{\lambda_c}u \cdot \left(\frac{x}{r}\right) \tag{21.60}$$

The phase progression of equation (21.60) is linearly proportional to platform location u and scatterer along-track location x. Figure 21-22a shows the form of equation (21.60) for three scatterers. The scatterer at broadside ($x = 0$) has no phase change as the platform position changes, so it has a phase progression slope of zero; scatterers on either side of broadside, with positive and negative x values, have positive and negative slopes.

The rate of change in phase as the platform moves can be examined by taking the derivative of the phase progression function with respect to platform position:

$$k_u \equiv \frac{\partial}{\partial u}\Delta\psi(u) \tag{21.61}$$

The term k_u in equation (21.61) is *spatial frequency*, the rate of change in phase angle in radians for a change in platform along-track position in meters with units of radians per meter. Spatial frequency is also sometimes known as *wavenumber*.

Spatial frequency is closely related to the more widely referenced temporal frequency, also known as Doppler, which has units of cycles per second (Hz) or radians per second.

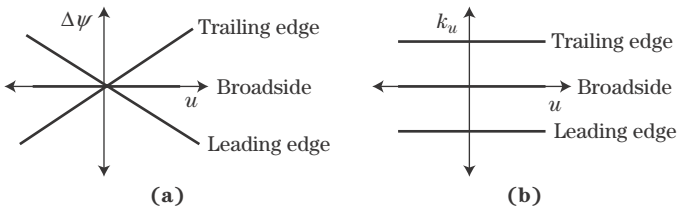

FIGURE 21-22 ■ In the DBS model, (a) phase progressions are approximately linear over the dwell, with slope mapping to cross-range location, and (b) spatial frequencies (Doppler) are approximately constant over the dwell, with frequency mapping to cross-range location.

When collecting SAR data against stationary scatterers, any change in phase from a scatterer from pulse to pulse is due solely to the change in the location of the platform. Therefore, there is a unique mapping of spatial frequency (wavenumber) to temporal frequency (Doppler) that is determined by the along-track sample interval and radar PRF, which in turn are related by the platform speed. Specifically, Doppler frequency is proportional to spatial frequency times the along-track speed of the platform v

$$f_d = -\frac{1}{2\pi} k_u v \tag{21.62}$$

where the factor of $1/2\pi$ puts the result in units of hertz.

The SAR community prefers spatial over temporal frequency because the former provides a more convenient measure of data and image properties. The amplitude and phase of the return from a scatterer are determined by the slant range from the platform to the scatterer. Slant ranges are a function of platform location, as indicated by the form of the PSR. In short, data records are a function of not *when* the radar measurement was made but from *where* the measurement was made. This dependency on position, not time, encourages the use of spatial frequencies.

Using the expression for phase progression in equation (21.60) in the definition of spatial frequency of equation (21.61) gives

$$k_u = -\frac{4\pi}{\lambda_c}\left(\frac{x}{r}\right) \tag{21.63}$$

For a fixed cross-track range r a scatterer has a constant spatial frequency over the dwell (i.e., for all u), as depicted in Figure 21-22b. The precise value depends on the cross-range location x. The frequency is highest for scatterers on the trailing edge of the antenna mainbeam (negative x), is zero for objects at broadside ($x = 0$) and is lowest for returns on the leading edge of the beam (positive x).

21.5.4 DBS Image Formation

The property that scatterers have constant spatial frequency over the dwell makes DBS image formation straightforward. As discussed in detail in Chapter 17, the Fourier transform is a convenient tool for analyzing the frequency content of a signal. The Fourier transform of a spatially sampled signal $s(u)$ to spatial frequency $S(k_u)$ takes the form

$$S(k_u) \equiv \int_{-\infty}^{\infty} s(u) e^{-jk_u u} du \tag{21.64}$$

For DBS this one-dimensional transform is applied to the two-dimensional raw SAR data by operating over the pulse history in each range bin, on a range bin by range bin basis. Mathematically, this can be written as

$$D(k_u, t) \equiv \int_{-\infty}^{\infty} d(u, t) e^{-jk_u u} du \tag{21.65}$$

so that range (fast time t) is transparent to the function. The output D is a two-dimensional complex function of time and spatial frequency. These dimensions map to scene position

via the following relationships:

$$t = \frac{2R}{c} = \frac{2\sqrt{x^2 + r^2}}{c} \tag{21.66}$$

$$k_u = -\frac{4\pi}{\lambda_c}\left(\frac{x}{r}\right) \tag{21.67}$$

Now assume that the scene center is far from the platform and the cross-range extent is limited so that $x \ll r$, and the down-range scene extent is small enough that its influence on spatial frequency can be ignored. Using r_0 for the cross-track range to scene center, equations (21.66) and (21.67) can be approximated as

$$t \approx \frac{2}{c} r \tag{21.68}$$

$$k_u \approx -\frac{4\pi}{\lambda_c}\left(\frac{x}{r_0}\right) \tag{21.69}$$

With these approximations, the final SAR image $f(x, r)$ can be formed via a simple linear rescaling of the axes of the fast-time/spatial-frequency data:

$$f(x, r) = D\left[\, k_u\left(-\frac{\lambda_c r_0}{4\pi}\right) \to x,\ t\left(\frac{c}{2}\right) \to r \,\right] \tag{21.70}$$

The DBS image formation procedure, a spatial Fourier transform over the pulse history followed by mapping of the data into the scene coordinates, is summarized in Figure 21-23.

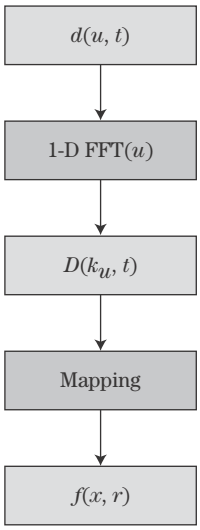

FIGURE 21-23 ■ DBS processing performs a spatial Fourier transform over the pulse history followed by mapping the data into scene coordinates.

21.5.5 DBS, Doppler, and the PSR

In the preceding two sections the PSR and a lengthy mathematical development were used to derive something that was already understood from consideration of the Doppler cone angle (θ_{cone}): a coarse SAR image can be formed by a one-dimensional Fourier transform of the data in each range bin. Indeed, the PSR derivation can be taken further to reproduce the Doppler relationship. Starting with equation (21.63),

$$k_u = -\frac{4\pi}{\lambda_c}\left(\frac{x}{r}\right)$$

and noting that the ratio (x/r) equals the tangent of the azimuth angle, which is approximately equal to the sine of the azimuth angle for small angles, gives

$$\frac{x}{r} = \tan\theta \approx \sin\theta$$

Spatial frequency then becomes

$$k_u \approx -\frac{4\pi}{\lambda}\sin\theta \tag{21.71}$$

The mapping between spatial frequency Doppler frequency is, from equation (21.62),

$$k_u = -\frac{2\pi}{v} f_d$$

Substituting this expression into equation (21.71) reproduces equation (21.10),

$$f_d \approx \frac{2v}{\lambda} \sin\theta \tag{21.72}$$

the relationship that is at the heart of the SAR Doppler paradigm. This development shows that the PSR can be used to develop and justify the Doppler filtering approach to SAR imaging.

21.5.6 DBS Example

Simulated data are now used to demonstrate the DBS image formation procedure. In this example the modeled radar and collection geometry have the following characteristics:

- Carrier frequency = 9.6 GHz.
- RF bandwidth = 3 MHz.
- Integration angle = 0.02°.
- Resolution = 50 meters (both dimensions).
- Number of along-track sample points (pulses) = 80.
- Range to scene center = 50 km.

Figure 21-24 contains diagrams of the collection geometry; note that the coordinate system origin is assigned to the center of the scene and not the platform location in these figures. The scene of interest, approximately 4 km × 4 km, appears to the right of Figure 21-24a, with the data acquisition locations at the far left. The axes ratio is distorted in Figure 21-24a to show both the scene and the platform positions. The synthetic aperture is relatively short so that the collection points all fall on top of one another in the diagram. The scene to be imaged is made up of five point scatterers whose locations are more easily discerned in the undistorted diagram in Figure 21-24b. One target is at the scene center, with the remaining targets distributed over down-range and cross-range.

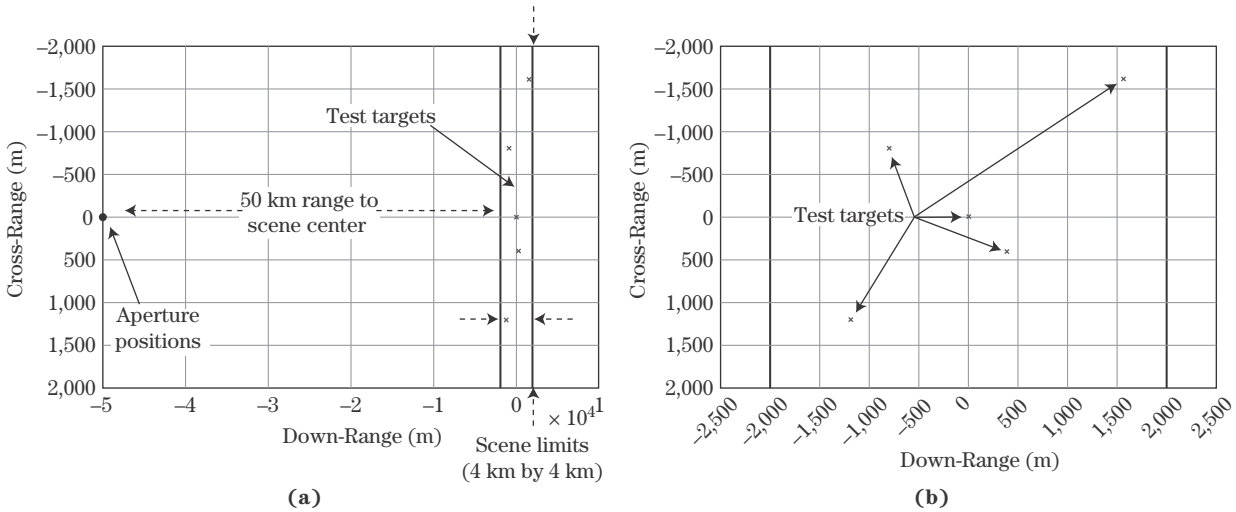

FIGURE 21-24 ■ Simulated DBS geometry emphasizes (a) the overall collection geometry, and (b) point scatterer locations in the scene of interest.

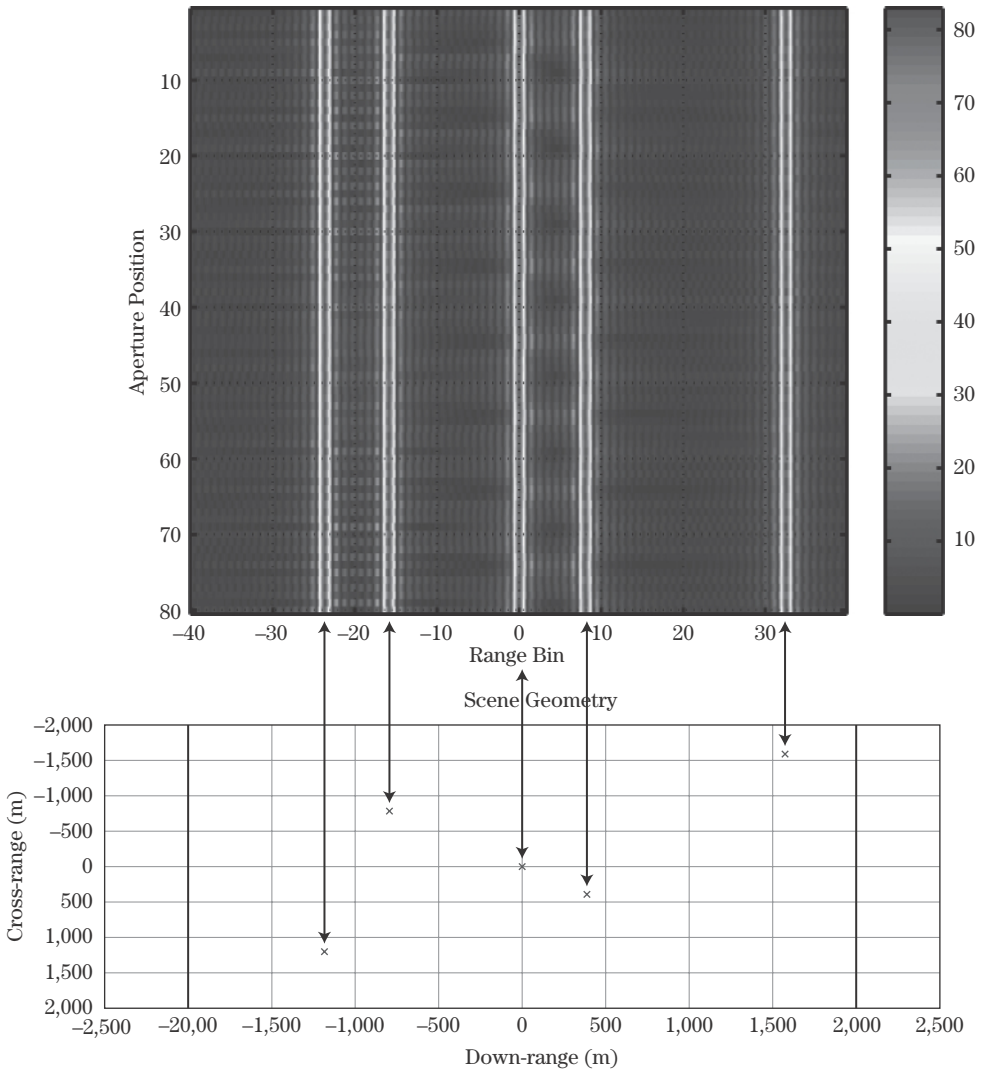

FIGURE 21-25 ■ Mapping of HRR profiles in the raw data to scatterer locations in the scene of interest.

An image of the magnitude of the recorded returns appears in Figure 21-25. The image shows the range-compressed raw data $d(u, t)$ with u given by aperture position number along the axis and t in the form of range bins numbered with respect to scene center. There are five point scatterer returns, one for each of the targets in the scene. For example, the return from the target at scene center appears at range bin number zero in Figure 21-25. Consistent with the assumption made under DBS imaging, the PSRs are confined to the same range bin over the collection.

Not shown in Figure 21-25 is the phase information. Figure 21-26 corresponds to the magnitude image in Figure 21-25 but indicates phase contribution by displaying the real part of the complex data $d(u, t)$. For example, the return in range bin zero displays no bipolar (positive and negative) fluctuations over the dwell, implying a constant phase and therefore zero Doppler and a cross-range location of zero. The other scatterers, in contrast, show some bipolar fluctuations. Low-frequency fluctuations are evidence of small Doppler (spatial frequency) and a location near the scene centerline, while higher frequencies reflect larger displacements. (The imaginary part of $d(u, t)$, not shown in Figure 21-26, has the

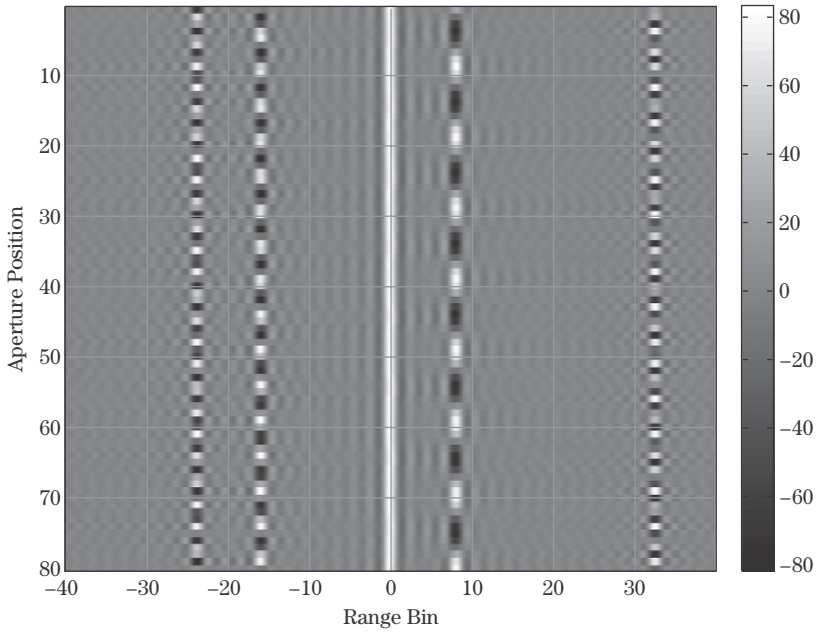

FIGURE 21-26 ■ Real part of the HRR profiles, with positive voltages in white and negative voltages in black, indicates phase changes over the dwell and, therefore, Doppler frequency.

same fluctuations frequencies as the real part, but the relative phasing between the real and imaginary components determines to which side of the centerline a scatterer falls.)

By Fourier transforming over the pulse history in each range bin (the columns in Figures 21-25 and 21-26), the linear phase signal of each scatterer is concentrated into a single frequency bin, which is then mapped to cross-range. The resulting DBS intensity image appears in Figure 21-27 on a decibel scale. The point responses in the image faithfully reproduce the true scatterer locations in Figure 21-24b. The target range Doppler functions show the two-dimensional "sinc" $(\sin x/x)$ response commonly observed in Fourier analysis.

21.5.7 DBS Limitations

The DBS approach to image formation is easy to implement, consisting primarily of a Fourier transformation over each compressed range bin, which can be performed in a computationally efficient manner through application of the fast Fourier transform (FFT) algorithm. (See Chapter 17 for details on the FFT.) However, DBS is a suitable image formation algorithm only under tightly restrictive conditions. Recall the series of assumptions and approximations made to derive DBS from the PSR:

- Scatterer returns have the same hyperbolic form such that all returns are confined to a single range bin over the dwell.
- The hyperbolic form of the PSR is replaced with a quadratic form via the binomial approximation.
- A quadratic term in platform position u was neglected.
- The mapping from time and spatial frequency to along-track and cross-track location was simplified.

Figure 21-28 depicts an imaging geometry much more demanding than that used to demonstrate the DBS technique (Figure 21-24). Five scatterers are clustered into the scene

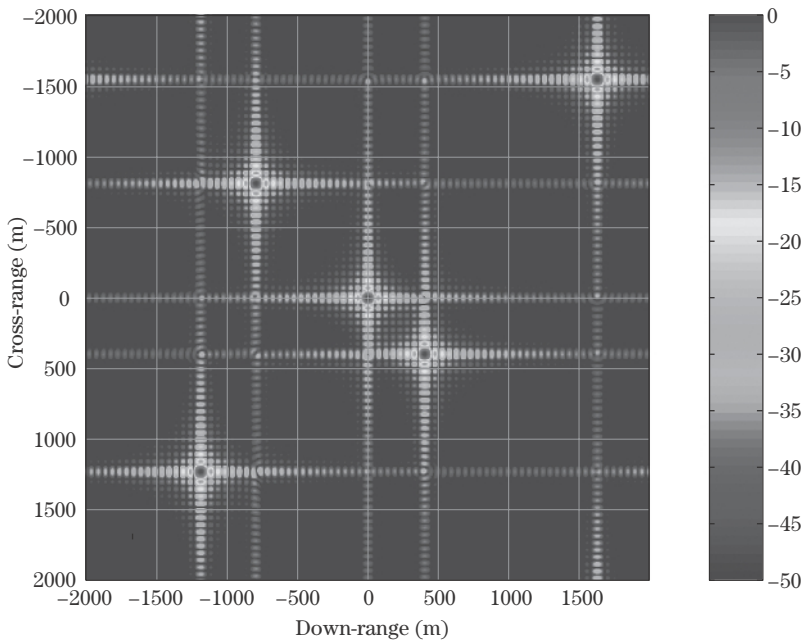

FIGURE 21-27 ■ DBS image of the simulated point targets.

of interest. For this simulation the radar and geometry parameters are

- Carrier frequency = 600 GHz.
- RF bandwidth = 750 MHz.
- Integration angle = 51°.
- Resolution = 0.2 meters (both dimensions).
- Number of along-track sample points (pulses) = 275.
- Range to scene center = 30 meters.

This example constitutes near-range imaging of a relatively large scene (compared with the range to the scene) with a low-frequency system employing a large RF bandwidth and wide integration angles to achieve fine resolution in down-range and cross-range. Figure 21-29 shows the real part of the resulting raw range-compressed data. The full hyperbolic form of the target PSRs is readily apparent. Target returns are not constrained to one range but

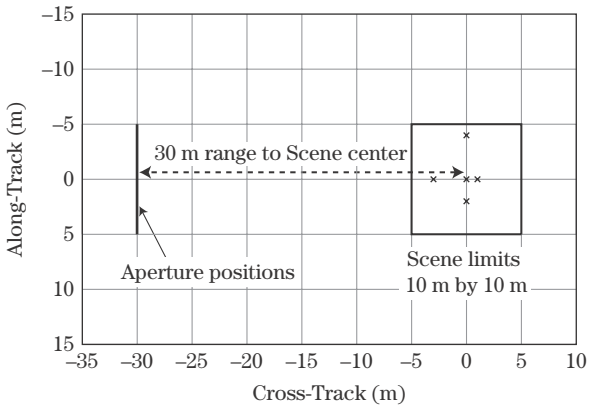

FIGURE 21-28 ■ A challenging, near-range collection geometry.

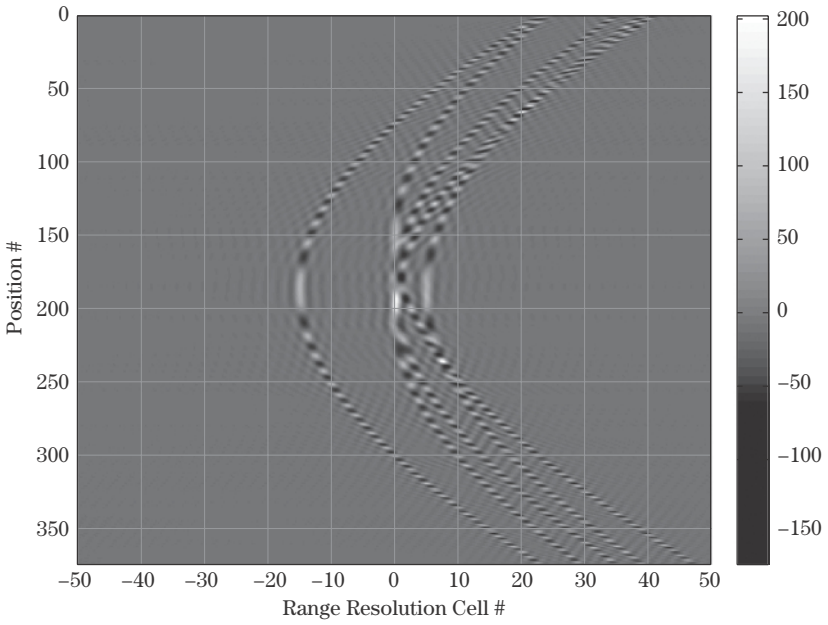

FIGURE 21-29 ■ Real part of the HRR profiles for the near-range collection. Tremendous range migration and higher-order phase modulations are apparent in the raw data.

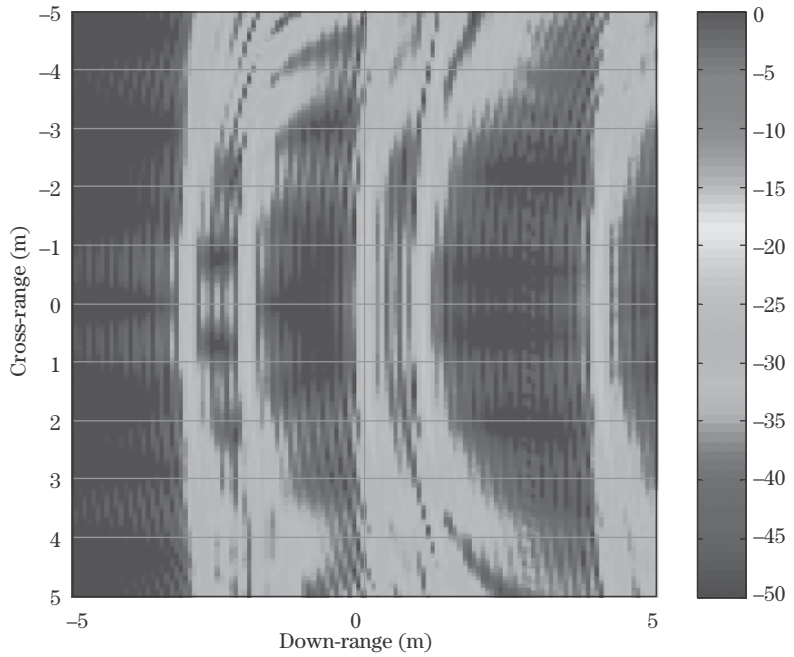

FIGURE 21-30 ■ The DBS image of the near-range point targets is distorted and unusable.

instead migrate over many range bins. A careful comparison of the returns reveals slightly different hyperbolic forms for scatterers at different down-range locations. The bipolar fluctuations of the PSRs indicate not linear phase (constant Doppler) or even quadratic phase but a complicated history consistent with the full hyperbolic PSR. Applying this data to DBS results in an image, provided in Figure 21-30, so terribly distorted and defocused as to be unusable.